ANS Reprint

DIVERTOR SYSTEMS

KEYWORDS: *magnetohydrodynamics, liquid-metal divertor, open channel flow*

STUDY OF FULLY DEVELOPED, LIQUID-METAL, OPEN-CHANNEL FLOW IN A NEARLY COPLANAR MAGNETIC FIELD

NEIL B. MORLEY and MOHAMED A. ABDOU
University of California, Los Angeles
Mechanical and Aerospace Engineering Department
43-133 Engineering IV, Los Angeles, California 90095-1597

Received August 10, 1995
Accepted for Publication June 9, 1996

Fully developed, gravity-driven flow in an open channel of arbitrary electrical conductance and orientation to an applied magnetic field is investigated. The formulation of the model equations and the numerical solution methodology are described in detail. Numerical solutions of the model equations for the flow velocity profile, induced magnetic field profile, and the uniform film height as a function of Hartmann number, field angle, flow rate, and channel conductivity are presented and discussed. The parameter ranges explored are those most representative of tokamak divertor surface protection schemes, where the field is predominantly coplanar in orientation. The formation of jets in velocity and the occurrence of abrupt jumps in uniform film height are seen as the wall conductance increases. Regimes where the flow is dominated by the smaller transverse field component instead of the larger coplanar field are also observed. Simple analytic relations predicting the film height are given for the different flow regimes.

I. INTRODUCTION

The utilization of a flowing liquid-metal film as a continuously replenished plasma contact surface has been around for some time[1] but is attracting more interest because no acceptable solid surface divertor design has yet evolved that is capable of withstanding the intense heat and particle fluxes of a fusion power reactor. Before the liquid-metal film concept can seriously be considered as an option for future tokamaks, the behavior of such a film in the environment of a tokamak divertor must be determined. This environment includes, among other things, the presence of strong, nonuniform, time-varying magnetic fields; large gradients in temperature; and plasma contact at the free surface. As an initial step in the validation process, a more basic understanding of open-channel, magnetohydrodynamic (MHD) flows in fusion-relevant geometries must be developed.

Early work on liquid-metal MHD, thin-film flow was performed by Alpher et al.[2] in the limit of wide-channel flow and in a transverse (see Fig. 1 for clarification) magnetic field. Much later, Walker[3] derived different solutions in the purely coplanar magnetic field orientation, and Hays and Walker[4] presented more detailed solutions of the transverse case than Alpher. All these studies were motivated by applications in the metals-processing area. In terms of fusion divertors, most model development and experiments utilize the quasi-coplanar field geometry because of the assumed dominance of the large toroidal field for a poloidally flowing divertor film. Most recent models[5–7] assume the applied field to be purely coplanar and then simplify the governing equations with the assumption of a Hartmann distribution of velocity across the channel.

In this work, neither of these assumptions is made. We investigate fully developed, two-dimensional film flow in a channel of arbitrary electrical conductance and a perpendicular applied magnetic field of arbitrary orientation. Sections II and III present the model equations and describe the numerical solution methodology. Section IV gives results of the model predictions for a variety of cases. Major conclusions are summarized in Sec. V.

It is the purpose of this paper to present a systematic study of the effects of different governing parameters on the open-channel flow fields and the uniform flow height. Separate papers expound in more detail on the fusion applications of this work[8] and the mathematical description of the flow,[9] although the reader is warned that there are some slight differences in the symbols and terminology of these companion papers. A more complete treatment of all details is available in the first author's dissertation.[10]

In addition, the reader is also referred to Kudrin et al.,[11] where an alternate numerical solution to this problem is reported.

II. FLOW EQUATIONS

The flow of liquid metal in a magnetic field is governed by the equations of magnetohydrodynamics, which include the Navier-Stokes equation of momentum conservation, the mass and current conservation equations, Ohm's law, and Maxwell's equations:

$$\frac{\partial \boldsymbol{v}}{\partial t} + (\boldsymbol{v}\cdot\nabla)\boldsymbol{v} = -\frac{1}{\rho}\nabla p + \nu\nabla^2\boldsymbol{v} + \boldsymbol{g} + \frac{\boldsymbol{j}\times\boldsymbol{B}}{\rho} \ , \quad (1)$$

$$\nabla\cdot\boldsymbol{v} = 0 \ , \quad \nabla\cdot\boldsymbol{j} = 0 \ , \quad (2)$$

$$\boldsymbol{j} = \sigma(\boldsymbol{E} + \boldsymbol{v}\times\boldsymbol{B}) \ , \quad (3)$$

and

$$\nabla\times\boldsymbol{B} = \mu\boldsymbol{j} \ , \quad \nabla\times\boldsymbol{E} = -\frac{\partial \boldsymbol{B}}{\partial t} \ , \quad \nabla\cdot\boldsymbol{B} = 0 \ , \quad (4)$$

where $\boldsymbol{v}$, $\boldsymbol{j}$, $\boldsymbol{E}$, and $\boldsymbol{B}$ are, respectively, the velocity, current density, electric field, and magnetic induction vectors. The symbols $\boldsymbol{g}$ and p are the acceleration of gravity and the pressure, while σ, ρ, ν, and μ are the electrical conductivity, mass density, kinematic viscosity, and magnetic permeability of the liquid metal, respectively. The constancy of these material properties is assumed throughout this work (see Nomenclature on p. 152). Other assumptions implicit in these equations are the incompressibility of the fluid and a negligible displacement current, $\epsilon(\partial \boldsymbol{E}/\partial t)$, in Ampere's law, Eq. (4a). The so-called induction equation is obtained by taking the curl of Ohm's law, Eq. (3), and using Eq. (2b), Eq. (4b), and some vector identities:

$$\frac{\partial \boldsymbol{B}}{\partial t} = \nabla\times\boldsymbol{v}\times\boldsymbol{B} + \frac{1}{\sigma\mu}\nabla^2\boldsymbol{B} \ . \quad (5)$$

This equation is more commonly used in formulations that solve for the induced magnetic field instead of the current density.

The typical quasi-coplanar geometry is shown in Fig. 1. Here the magnetic field is nearly aligned with the coplanar direction having unit vector $\hat{z}$, lying in the plane of the film but perpendicular to main flow direction. The $\hat{x}$ unit vector points in the direction of dominant fluid flow and is termed longitudinal. The $\hat{y}$ unit vector denotes the coordinate normal to the backplate and is named the transverse direction. Other definitions include h as the film height measured along y, θ denoting the angle of the backplate to the horizon (measured positive for downward sloping chutes), α as the angle of the magnetic induction to $\hat{z}$, and finally a as the channel width with the chute walls located at $\pm a/2$. This type of flow

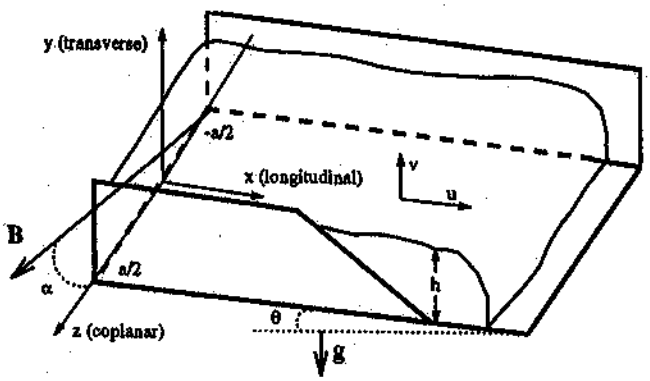

Fig. 1. Geometry of quasi-coplanar liquid-metal film flow.

is indicative of poloidally flowing divertor films where the main toroidal field component is largely aligned with $\hat{z}$. Any small component of the field in the $\hat{x}$ direction is discarded in this fully developed analysis, so that the applied field is given by $\boldsymbol{B}^a = (0, B_y^a, B_z^a) = B^a(0, \sin\alpha, \cos\alpha)$.

These basic MHD equations are simplified by treating the case of laminar, fully developed, open-channel flow assuming a uniform film height over the cross section of the channel. As a consequence of the fully developed assumption, the total pressure dependence on y is hydrostatic, and the height of the flow is no longer changing as it proceeds down the channel. The velocity has only a longitudinal component $\boldsymbol{v} = (u,0,0)$ as a result of the driving force of gravity. The induced magnetic field is also reduced to only one component in the longitudinal direction, $\boldsymbol{B}^i = (b_x,0,0)$. The assumption of a flat surface over a cross section of the flow $\partial h/\partial z = 0$ requires that the magnitude of the induced magnetic field is small compared with the applied field. This condition can be assumed now and checked against the results for any given dimensional case.

The application of these simplifying assumptions reduces Eqs. (1) through (5) to the following system in terms of the velocity, induced magnetic field, volumetric flow rate, and the uniform film height:

$$\nabla_\perp^2 u + \frac{1}{\rho\mu\nu}(\boldsymbol{B}^a\cdot\nabla_\perp)b_x = -\frac{g\sin\theta}{\nu} \ , \quad (6)$$

$$\nabla_\perp^2 b_x + \mu\sigma(\boldsymbol{B}^a\cdot\nabla_\perp)u = 0 \ , \quad (7)$$

and

$$\int_{-a/2}^{a/2}\int_0^h u\,dy\,dz = Q \ , \quad (8)$$

where $\nabla_\perp = (0, \partial/\partial y, \partial/\partial z)$ operates only on the components perpendicular to the flow direction. The solution space for these equations can be seen in Fig. 2, along with the graphical representations of different flow

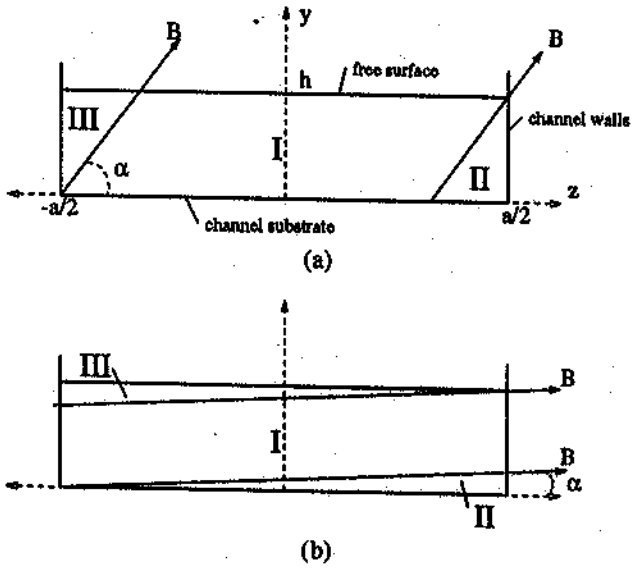

Fig. 2. Channel flow regions and regimes for oblique magnetic field incidence: (a) regime 2 and (b) regime 3.

regimes and regions defined later. The constant flow rate condition, Eq. (8), is given as the third equation of the fully developed model formulation. Equation (8) is coupled with Eqs. (6) and (7) through the boundary conditions since h is the upper limit of the solution space for the velocity and induced field profiles. If h is assumed a priori, then Eq. (8) is needed only to compute the flow rate that results from such a uniform film height.

The boundary conditions for the velocity assume no slip on the channel walls and no shear stress at the free surface,

$$u = 0 \quad \text{at } y = 0 \text{ or } z = \pm a/2 \tag{9}$$

and

$$\frac{\partial u}{\partial y} = 0 \quad \text{at } y = h \ . \tag{10}$$

At the channel walls, the so-called thin conducting wall approximation is employed for the induced field,

$$\left(\frac{\sigma_s a_s}{\sigma_f}\right)\frac{\partial b_x}{\partial z} \pm b_x = 0 \quad \text{at } z = \pm a/2 \tag{11}$$

and

$$\left(\frac{\sigma_b a_b}{\sigma_f}\right)\frac{\partial b_x}{\partial y} - b_x = 0 \quad \text{at } y = 0 \ , \tag{12}$$

while at the free surface we have

$$b_x = 0 \quad \text{at } y = h \ . \tag{13}$$

Here the subscripts f, b, and s refer to the fluid, bottom wall, and the side walls, respectively, while a_b and a_s denote the wall thicknesses. Equations (11) and (12) are derived from the electromagnetic equations[12] by treating each channel wall as an infinitely thin conductor with no voltage difference over the thickness, and no leakage from the exterior, of the wall. Equations (11) and (12) are accurate provided that the resistance between the inside and outside surfaces of each wall is small compared with the resistance of the entire current path through the walls.

Equations (6), (7), and (8) and the boundary conditions are normalized using the following characteristic quantities and dimensionless parameters:

$$y_* = h \ , \tag{14}$$

$$z_* = a/2 \ , \tag{15}$$

$$u_* = (a/2)^2 g \sin\theta/\nu \ , \tag{16}$$

$$b_* = u_* \mu(\sigma\nu\rho)^{1/2} \ , \tag{17}$$

$$Q_* = 2(a/2)^2 u_* \ , \tag{18}$$

$$\mathrm{Ha} = B^a(a/2)(\sigma/\rho\nu)^{1/2} \ , \tag{19}$$

$$\Phi_{s,b} = (a_{s,b}\sigma_{s,b})/[(a/2)\sigma] \ , \tag{20}$$

and

$$\beta = h/(a/2) \ . \tag{21}$$

Denoting the dimensionless variables with a tilde, the new set of equations is written as

$$\frac{\partial^2 \tilde{u}}{\partial \tilde{y}^2} + \beta^2 \frac{\partial^2 \tilde{u}}{\partial \tilde{z}^2} + \mathrm{Ha}\beta\left(\sin\alpha \frac{\partial \tilde{b}_x}{\partial \tilde{y}} + \beta\cos\alpha \frac{\partial \tilde{b}_x}{\partial \tilde{z}}\right) = -\beta^2 \ , \tag{22}$$

$$\frac{\partial^2 \tilde{b}_x}{\partial \tilde{y}^2} + \beta^2 \frac{\partial^2 \tilde{b}_x}{\partial \tilde{z}^2} + \mathrm{Ha}\beta\left(\sin\alpha \frac{\partial \tilde{u}}{\partial \tilde{y}} + \beta\cos\alpha \frac{\partial \tilde{u}}{\partial \tilde{z}}\right) = 0 \ , \tag{23}$$

and

$$\frac{\beta}{2}\int_{-1}^{1}\int_{0}^{1} \tilde{u}\, d\tilde{y}\, d\tilde{z} = \beta\tilde{u}_{ave} = \tilde{Q} \ . \tag{24}$$

The choice of this normalization leaves the differential operators on the left side of Eqs. (22) and (23) identical. Adding and subtracting the two equations reforms this system into

$$\frac{\partial^2 \omega_\pm}{\partial \tilde{y}^2} + \beta^2 \frac{\partial^2 \omega_\pm}{\partial \tilde{z}^2} \pm \mathrm{Ha}\beta\left(\sin\alpha \frac{\partial \omega_\pm}{\partial \tilde{y}} + \beta\cos\alpha \frac{\partial \omega_\pm}{\partial \tilde{z}}\right) = -\beta^2 \ , \tag{25}$$

where $\omega_\pm = \tilde{u} \pm \tilde{b}_x$. Although the equations for ω_+ and ω_- are decoupled, the new variables are related now through coupled boundary conditions. These new boundary conditions are

$$0 = \{\omega_+ + \omega_-\}_{\tilde{y}=0 \text{ or } \tilde{z}=\pm 1} , \quad (26)$$

$$0 = \left\{\frac{\partial \omega_+}{\partial \tilde{y}} + \frac{\partial \omega_-}{\partial \tilde{y}}\right\}_{\tilde{y}=1} , \quad (27)$$

$$0 = \{\omega_+ - \omega_-\}_{\tilde{y}=1} , \quad (28)$$

$$0 = \left\{\Phi_s \frac{\partial}{\partial \tilde{z}}(\omega_+ - \omega_-) \pm (\omega_+ - \omega_-)\right\}_{\tilde{z}=\pm 1} , \quad (29)$$

and

$$0 = \left\{\frac{\Phi_b}{\beta}\frac{\partial}{\partial \tilde{y}}(\omega_+ - \omega_-) - (\omega_+ - \omega_-)\right\}_{\tilde{y}=0} . \quad (30)$$

With these boundary conditions the nondimensional system is complete. The governing parameter set is effectively reduced to Ha, $\Phi_{s,b}$, α, and either $\tilde{Q}$ or β. From this point on, the tildes will be dropped from the equations for convenience.

III. NUMERICAL SOLUTION

The simple grid constructed for this problem is an unequally spaced, rectangular mesh with fine grid spacing used near the walls and a larger spacing in the interior. The cell size is varied gradually in between so that there is no abrupt change from small to large, with a maximum ratio of size from one cell to the next of <1.5. The total number of grid points and the grid spacing in the $\hat{z}$ direction can be varied independently from that in the $\hat{y}$ direction. The cell size is denoted as δ, where $\delta_y[i]$ specifically denotes the cell size in the $\hat{y}$ direction between grid points i and $i + 1$. A similar notation is used for $\hat{z}$ direction.

Equation (25) is identical in form to the standard heat conduction/convection equation,

$$\alpha_d \nabla^2 T - (\boldsymbol{v}\cdot\nabla)T = S , \quad (31)$$

with anisotropic thermal diffusivity (α_d) and heat sources denoted by S. The role of the convection velocity is played by the magnetic field terms,

$$\alpha_{dy} = 1 , \quad \alpha_{dz} = \beta^2 , \quad (32)$$

$$v_y = \pm \mathrm{Ha}\beta \sin\alpha , \quad v_z = \pm \mathrm{Ha}\beta^2 \cos\alpha , \quad (33)$$

and

$$S = -\beta^2 . \quad (34)$$

As is known from the study of Eq. (31), the first-order derivatives are not accurately represented by second-order central differences when the cell Peclet number, $\mathrm{Pe} = v\delta/\alpha_d$, is >2 (Ref. 13). Considering Eq. (25), an analogous situation arises where an equivalent Pe can be determined from the quantities listed in Eqs. (32) and (33). Since the medium is anisotropic, a different Pe will be needed for each first-order derivative and, due to sign reversal, for both the ω_+ and ω_- equations as well. The Pe for each combination is

$$\mathrm{Pe}_{y+}(i) = \mathrm{Ha}\beta \sin\alpha\delta_y[i] , \quad (35)$$

$$\mathrm{Pe}_{z+}(j) = \mathrm{Ha} \cos\alpha\delta_z[j] , \quad (36)$$

$$\mathrm{Pe}_{y-}(i) = \mathrm{Ha}\beta \sin\alpha\delta_y[i-1] , \quad (37)$$

and

$$\mathrm{Pe}_{z-}(j) = \mathrm{Ha} \cos\alpha\delta_z[j-1] , \quad (38)$$

where the Peclet number subscripts denote first the respective derivative and then the $\omega_\pm$ equation to which they apply. For small values of Pe, both the second- and first-order derivatives are discretized with second-order central differences. If the condition $\mathrm{Pe} > \mathrm{Pe}_{crit}$ is reached, then that particular first-order derivative is approximated with a combination of central difference and upwind scheme instead:

$$\left(\frac{\partial}{\partial y}\right)_{discrete} = \frac{\mathrm{Pe}_{crit}}{\mathrm{Pe}} \cdot \left(\frac{\partial}{\partial y}\right)_{c.d.} + \left(1 - \frac{Pe_{crit}}{Pe}\right) \cdot \left(\frac{\partial}{\partial y}\right)_{upwind} . \quad (39)$$

The upwind method used here is only first-order accurate with respect to the grid spacing but provides more physically realistic solutions than second-order central differences when Pe > 2. The value of Pe_{crit} should be ≤2 for a smooth transition from central to upwind differencing. The value of $\mathrm{Pe}_{crit} = 1.5$ is used in this work.

As discussed by Patankar[13] on p. 106 of his book, the occurrence of false diffusion when the grid is not aligned with the convection velocity in Eq. (33) is to be expected for this scheme. This will result in some smearing out of sharp gradients of $\omega_\pm$ perpendicular to field lines when $\alpha \neq 0$. This false diffusion is reduced by the use of the finest possible grid spacing in the interior region.

As seen from Eqs. (26) through (30), we have two coupled boundary conditions on each wall and at the free surface. One boundary condition contains derivatives, while the other condition is a Dirichlet condition. Here we use the derivative condition to define a ghost point outside the solution domain for either the ω_+ or ω_- equation and then the Dirichlet condition to fix the boundary value of the other equation. The particular $\omega_\pm$ equation to which the derivative condition is applied is selected to maximize the value multiplying $\omega[i,j]$ at the boundary point, increasing the diagonal dominance of the sparse discrete operator matrix and leading to stable solutions using iterative solution techniques. To satisfy this requirement then, ghost points are defined for the $y = 1$ and $z = 1$ boundaries of the ω_+ equation and the $y = 0$ and $z = -1$ boundaries of the ω_- equation.

The corners located at the free surface always obey the condition $\omega_{\pm} = 0$ since both u and b are zero regardless of wall conductivity. The corner at $[0,-1]$ is included in the solution space of the ω_- equation, but the corner at $[0,1]$ is included in neither (or both) solution spaces. This corner is computed separately from the regular solution process (described in the following paragraphs) to satisfy both boundary conditions and the induction equation.

The solution to the discretized set of equations and boundary conditions is obtained iteratively. The programs written (FDFF and FDBV) alternate by first solving the constant-z columns as tridiagonal systems while marching across the solution space rows and then by solving the constant-y rows as tridiagonal systems on the next pass. The direction of line marching is chosen from upwind to downwind to speed convergence. Ghost points and boundary points needed for each pass are updated immediately before the pass based on the latest iteration data. Convergence is tested by looking at the average grid residual and the maximum difference between passes. Testing has established the convergence criterion at

$$\frac{\max_{i,j}[\omega_{new}(i,j) - \omega_{old}(i,j)]}{\max_{i,j}[\omega_{new}(i,j)]} < 10^{-8} \qquad (40)$$

as satisfactory.

The FDFF code solves the problem with the value of β given and then, at the end, computes the Q from Eq. (24). FDBV solves for β as well, after each pass recomputing β from Eq. (24), using a given Q. FDFF converges faster as a result of the reduced number of variables in the solution set. The two codes give consistent answers to equivalent problems and accurately converge to known analytic solutions[3,9] in the limit of large or small β and in the limit of large Ha.

IV. RESULTS OF FULLY DEVELOPED MODEL

The numerical solution of Eqs. (22), (23), and (24) yields the values of the two scalar fields u and b at the discrete points on the solution grid and the single scalar value of either β or Q describing the flow as a whole. The response of these quantities to variations in the governing parameters Ha, α, $\Phi_{s,b}$, and either β or Q has been investigated by examining many solutions generated with the FDFF and FDBV codes. The range of Q variation considered in the following solutions is that most relevant to wide, thin-film flow, as needed to cover large divertor surfaces. The cases are presented in terms of increasing complexity and number of governing parameters. The general trends of the solutions as a function of these parameters are discussed and quantified.

IV.A. Zero Magnetic Field

We begin by looking at the velocity profile corresponding to the case of no magnetic field (Ha = 0) and wide, thin-film flow ($\beta \ll 1$), shown in Fig. 3. The flow is computed as laminar to compare with later cases laminarized by the field. In this limiting case, the parameters α and Φ no longer have any significance, and only the normalized flow rate Q influences the form of the solution. At relatively low flow rates, the computed value of β is small, tending to increase with increasing flow rate (see Fig. 4). In dimensionless form, the uniform film height is seen to be

$$\beta = (3Q)^{1/3} , \qquad (41)$$

when $\beta \ll 1$, agreeing with simple one-dimensional, analytic, open-channel solutions.

At small β, the viscous drag is almost entirely generated by the bottom wall, with the side walls exerting an effect only in a thin boundary layer of thickness β relative to the dimensionless width. As seen in Fig. 3, this results in a velocity profile independent of z over the majority of the channel. The constancy of the profile with z is what is meant by the wide-channel assumption, and it is a well-understood result in ordinary hydrodynamics (OHD). As the flow rate, and hence the value of β, increases, the side wall friction becomes greater until, at $\beta \approx 1$, the bottom wall and each side wall exert a drag of similar magnitude.

IV.B. Electrically Insulated Walls

With the magnetic field no longer zero, we begin by taking the electrical conductivity of the walls to be zero, thus eliminating $\Phi_{s,b}$ as governing parameters and forcing the electric current loops to remain completely within the liquid metal. This constraint tends to reduce

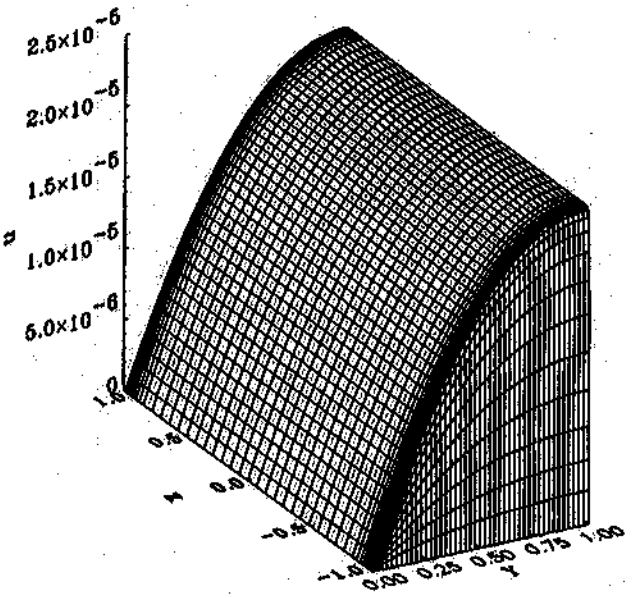

Fig. 3. Laminar velocity profile with Ha = 0 and $Q = 10^{-7}$.

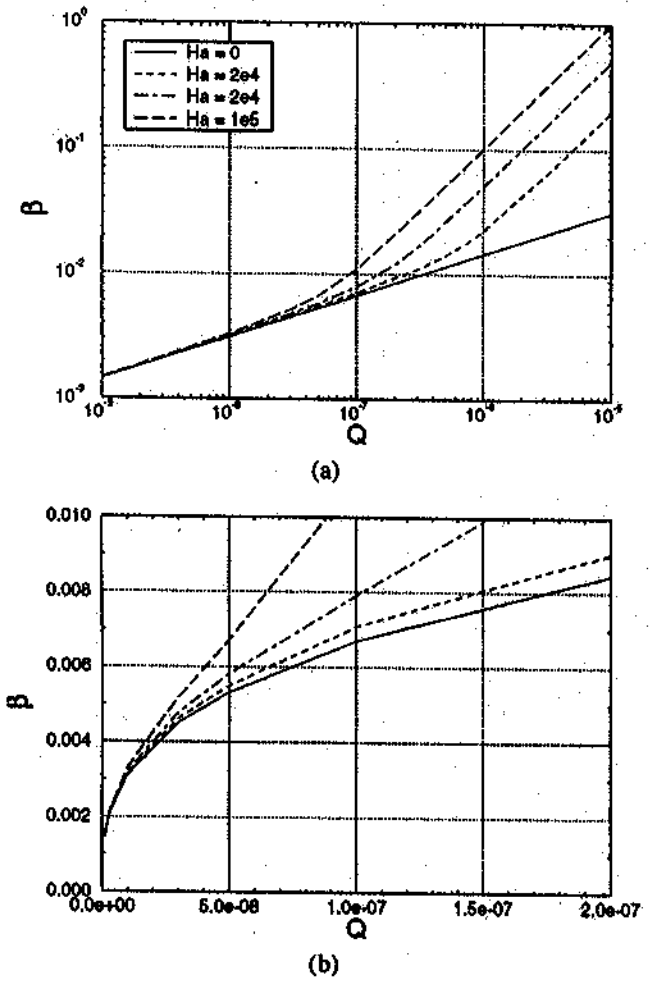

Fig. 4. Normalized film height as a function of flow rate and Hartmann number with (a) logarithmic and (b) linear axes.

the electromagnetic opposition to the flow as compared with cases with highly conducting walls. In addition, it is a simpler numerical problem to implement since $\omega_{\pm}$ are zero on all the channel walls, remaining coupled only at the free surface.

$\alpha = 0$ Case

With the field exactly aligned with $\hat{z}$ ($\alpha = 0$), the only new parameter considered, in comparison to the no-field case of Sec. IV.A, is the Hartmann number. Figure 5 shows the velocity and induced magnetic field profiles for various Q values at a characteristic fusion Ha. At low flow rates, the profiles are virtually indistinguishable from their zero-field counterparts. As the flow rate increases, the influence of the magnetic field has a greater effect on the fully developed profiles. This dependence is due to the increase in the value of β with increasing flow rate. As β increases, the ratio of the length over which the $\boldsymbol{v} \times \boldsymbol{B}$ electromagnetic force (EMF) acts relative to the total length of a current loop increases, indicating less relative resistance to current flow per unit EMF. Thus, an increase in the effect of the magnetic forces is seen, and a reduction in the hegemony of the viscous drag forces on the form of the velocity profile results. (Aside—for the electric current flowing along the contours on the right of Fig. 5, the electric circuit is completed through the Hartmann layers, which are fully resolved numerically but are visually lost in contours of this scale.)

Figure 4 graphically depicts the dependence of β on Ha and Q. We can see in both plots that the normalized film height becomes linear with Q when there is strong MHD interaction. In fact, the constant of proportionality is simply the Hartmann number:

$$\beta = Q\mathrm{Ha} \quad \text{or} \quad u_{ave} = \frac{1}{\mathrm{Ha}} \ . \tag{42}$$

This relation is the MHD equivalent of Eq. (41) but requires only significant MHD interaction (quantified in the following paragraphs) without any restrictions of β itself. The linearity of the film height with Ha is analogous to the linearity of pressure drop with Ha in fully developed, liquid-metal MHD duct flow with fixed flow rate.

Instead of simply the Hartmann number, we see that $\mathrm{Ha}\beta^2$ becomes the accurate ratio of magnetic to viscous forces, where this may have been guessed from the form of the governing equation, Eq. (25), with $\alpha = 0$. This parameter reduces to the common use of Ha in this role as β approaches unity for flows not elongated along the applied field. It can be seen from Fig. 4 that β deviates by ~5% from the OHD solutions at $\mathrm{Ha}\beta^2 \approx 1$ and that β becomes completely linear in the range of $\mathrm{Ha}\beta^2$ from 50 to 100. Using these two relations, together with Eqs. (41) and (42) to eliminate β, we can define the type of flow expected in terms of the initially given parameters Q and Ha:

$$0 < Q < \mathrm{Ha}^{-3/2}/3 \quad \text{OHD flow} \ ,$$

$$\mathrm{Ha}^{-3/2}/3 < Q < 10\mathrm{Ha}^{-3/2} \quad \text{transition , and}$$

$$10\mathrm{Ha}^{-3/2} < Q < \infty \quad \text{MHD core flow} \ .$$

As the flow rate is increased for a constant Ha (or Ha is increased for a constant Q), the effect of the magnetic field on the flow manifests as a flattening of the center region into an inviscid slug flow and the formation of boundary layers on the side walls, bottom wall, and free surface. The MHD interaction at lower flow rates affects the fluid region near the side walls, where the relative resistance to electric current flow is smallest. In this near-wall region, we see the beginning of Hartmann layer formation and the flattening of the near-wall core

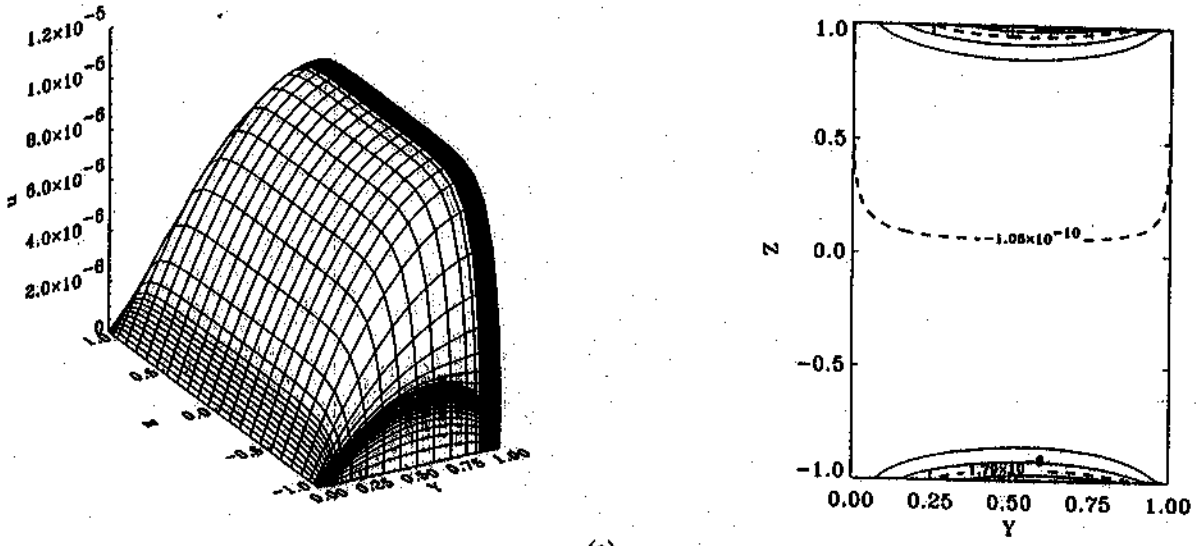

(a)

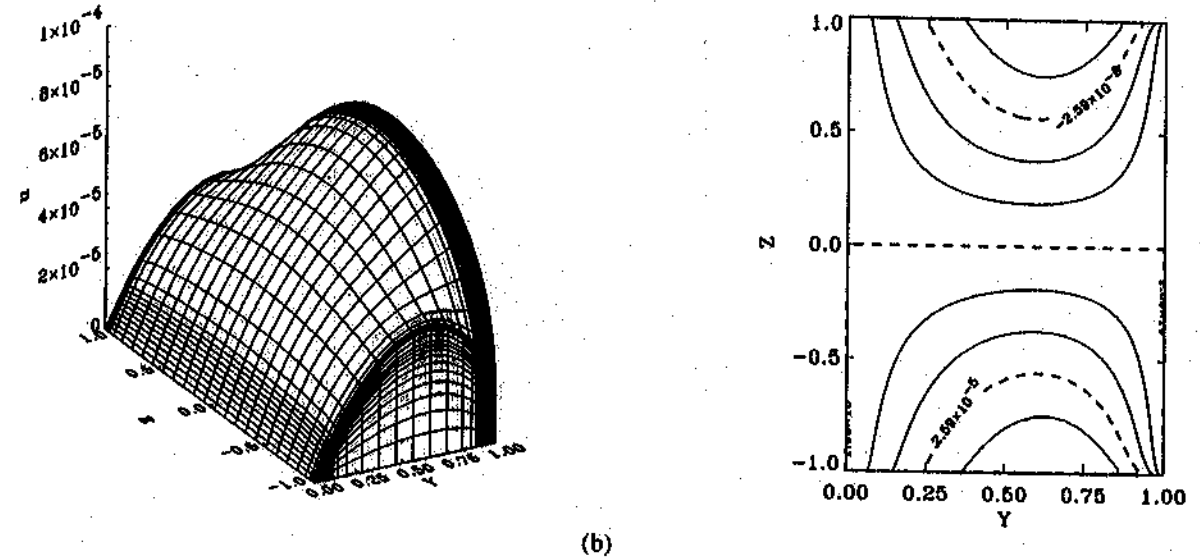

(b)

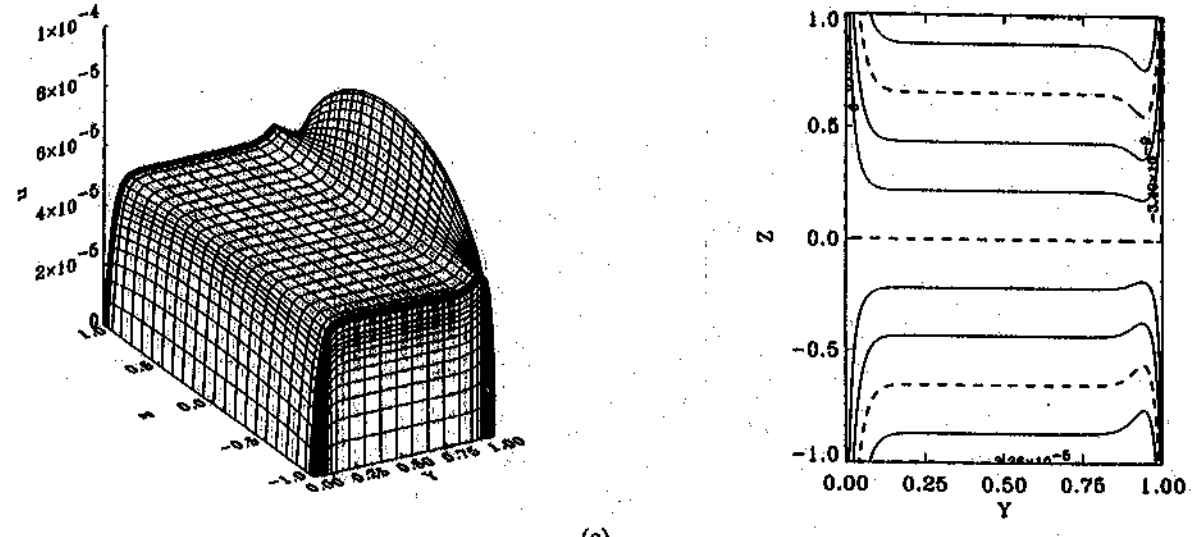

(c)

Fig. 5. Velocity and induced magnetic field profiles with Ha = 2×10^4 and Q = (a) 3×10^{-8}, (b) 10^{-6}, and (c) 10^{-5}.

flow, with currents circulating locally in the affected area. This current circulation is seen in the isocontours of the induced field, shown in Fig. 5a, which trace the current paths in the flow cross section.

As the flow rate (or Ha) increases further, the EMF generated in the interior region has enough strength to overcome the resistance of the long current closing paths from the center of the channel to the walls. Thus, the total current gradually increases, and the current distribution creeps inward until eventually it spreads out over the entire core region and becomes constant. The formation of the inviscid core region is complete at $Ha\beta^2 \approx 100$, the parallel layer thickness being $\sim 1/10$ the film height at this value of $Ha\beta^2$. After this point, no major changes in the velocity or the induced magnetic field profiles are observed with increases in Q, only the thinning of the boundary layers and thickening of the film height as the magnetic interaction increases.

The thickness of the Hartmann boundary layer is of the order Ha^{-1}, while that of the parallel layers is $(Ha\beta^2)^{-1/2}$. This difference in form between the two is due to the fact that lengths in the $\hat{y}$ and $\hat{z}$ directions are normalized with different characteristic lengths. For $\beta = 1$, they are the same as predicted for MHD channel flow.

The form of the parallel layer on the free surface, however, is different than that of a usual duct flow parallel layer. The absence of the no-slip boundary pulling the velocity to zero allows a jet to form. This jet has an almost parabolic distribution in $\hat{z}$ since at the free surface only viscous friction with the side walls restrains it. The region very near the free surface is magnetically unfettered since currents must turn parallel to the surface in order to close through the Hartmann layers on the side walls, leaving no current perpendicular to the applied magnetic field at this point. The jet then drags neighboring fluid, by virtue of the fluid viscosity, along with it, forming a parallel layer of finite thickness at the free surface. The peak velocity of the jet is $\sqrt{3} \cdot v_{core}$ for all $Ha\beta^2 > 100$. Walker's asymptotic solution[3] to this problem matches well to all these numerical results, including the form of the surface parallel layer.

$\alpha \neq 0$ *Case*

Looking now at the case where the applied magnetic induction vector is not perfectly aligned with the backplate of the channel, and thus there is a component of the field in the $\hat{y}$ direction, we note significant changes in the velocity and induced field profiles, as well as β, from their $\alpha = 0$ counterparts. Figure 6 shows a typical set of velocity and induced field profiles for several different values of Q, while Fig. 7 shows the β profiles as a function of Q for several Hartmann numbers.

From these plots we again see the now-familiar trend of the normalized film height to increase with Q. This trend, though, is amplified by the increasing magnitude of α. This amplification is explained by the fact that the field in the $\hat{y}$ direction, for a film elongated in $\hat{z}$, has a greater effect than a field of equal magnitude in the $\hat{z}$ direction. This is due to the greater length over which the $\boldsymbol{v} \times \boldsymbol{B}$ force acts to develop a larger EMF. It is the case in which the field is along the $\hat{y}$ direction that the work of Alpher et al.[2] is more directly analogous.

Despite the tendency of the $\hat{y}$ component of applied field to exert a stronger effect (drag) on the flow, the magnitude of this effect at the small angles α (characteristic of a poloidally flowing fusion divertor, the field is largely aligned with $\hat{z}$) is still somewhat limited. We are able to demarcate the flow into three regimes based on the level of interaction of the $\hat{z}$ and $\hat{y}$ components of the field. These will be referred to as regimes 1, 2, and 3. In addition, the flow area itself is divided into three separate regions I, II, and III. The flow regions are shown pictorially in Fig. 2 where region I is the central section, region II does not have a free surface border, and region III does border the surface.

Regime 1 looks like OHD flow (Fig. 3a). It is dominated in region I by the viscous drag of the bottom wall, with the MHD forces playing a role only in regions II and III, if even then. In fact, it is in most respects identical to the nonmagnetic case at small values of β.

Regime 2 is seen in Fig. 6a. Here the $\hat{y}$ component of the induced field dominates the behavior of the core, causing it to flatten out like a regular Hartmann profile with a viscous Hartmann layer on the channel backplate. The effect of the $\hat{z}$ component of the field is negligible in comparison to the $\hat{y}$ component except in regions II and III where the formation of Hartmann layers due to the B_z^a component can be seen on the $z = \pm 1$ side walls. The regions are separated by free shear layers, which are aligned with the field and extend outward from the channel corners. It should be noted that region II is not a mirror image of region III since the free surface provides asymmetrical boundary conditions for the two regions. Currents from region III seem to enter region I with little disturbance, while those entering region II turn toward the bottom wall and form two loops circulating in opposite directions.

Regime 3, pictured in Fig. 6c, is the case where the $\hat{z}$ component of the field dominates region I. It is attained as β continues to grow as a result of increasing Q, and the profiles begin to look like the $\alpha = 0$ case pictured in Fig. 5. The crossover between regimes 2 and 3 occurs at the β where a single field line intercepts both the lower left and upper right corners of the flow, $\beta = 2 \tan \alpha$, where

$$\beta < 2 \tan \alpha \quad \text{regime 2 flow} \tag{43}$$

and

$$\beta > 2 \tan \alpha \quad \text{regime 3 flow} \; . \tag{44}$$

At the transition point, region I disappears entirely, and only the two corner regions remain. In regime 3 flow,

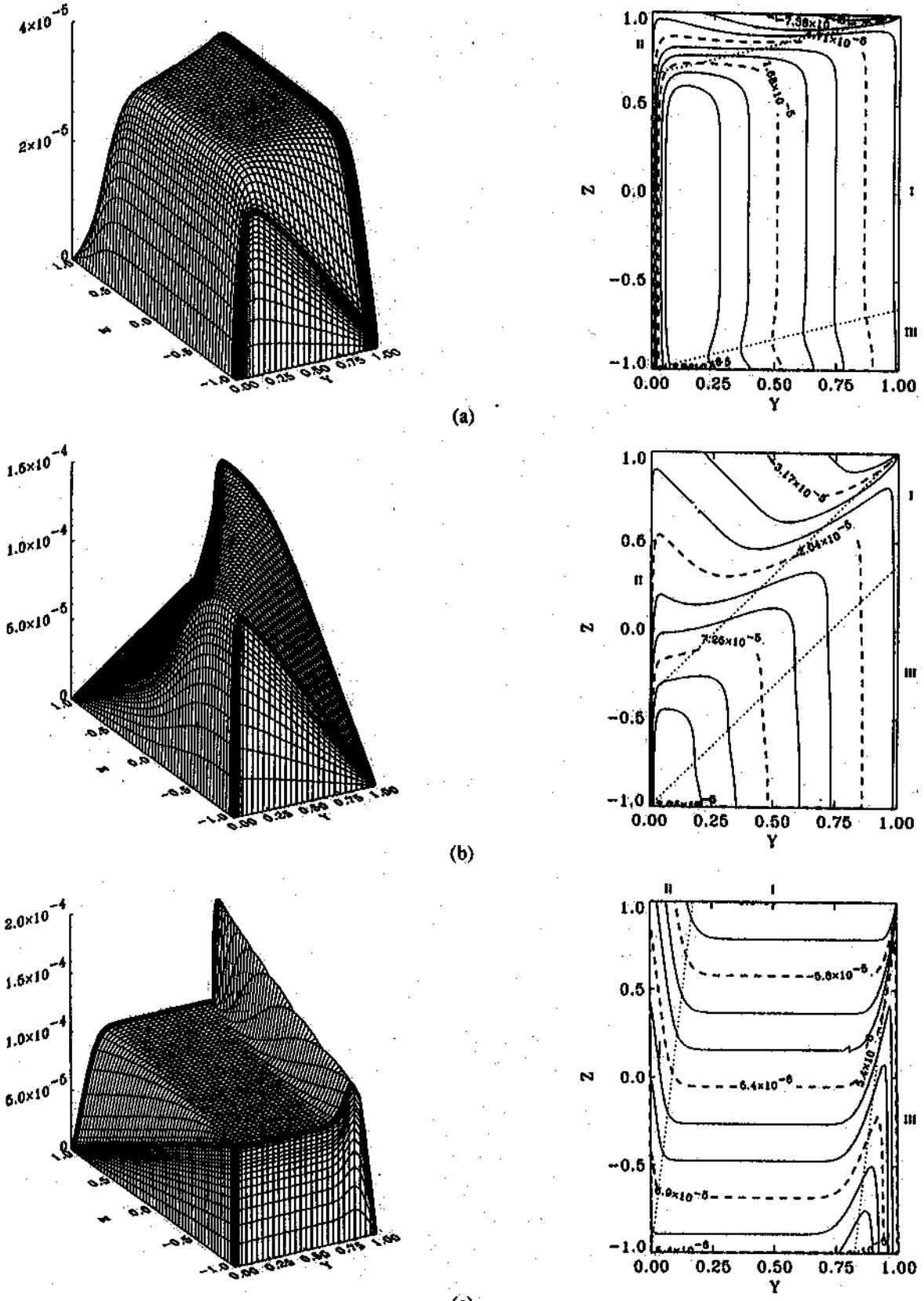

Fig. 6. Velocity and induced magnetic field profiles with Ha = 10^4, α = 5 deg, and $\beta(Q)$ = (a) 0.03 (8.9×10^{-7}), (b) 0.12 (10^{-5}), and (c) 1 (10^{-4}).

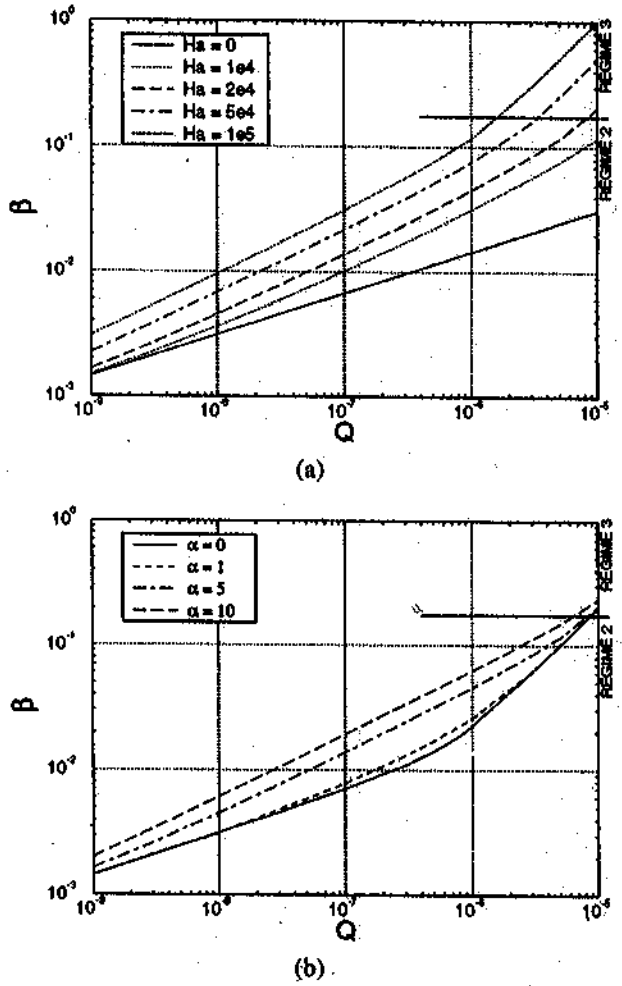

Fig. 7. Normalized film height as a function of flow rate for (a) various Ha at $\alpha = 5$ deg and (b) various α at Ha = 2×10^4. (The regime 2, 3 line is for the $\alpha = 5$-deg case only.)

then, region I no longer has a free surface boundary. A near transition flow is shown in Fig. 6b. It should be noted that not all regimes are reached for every Ha and α for the range of fusion-relevant flow rates that we have been using.

Some interesting characteristics of the flow regimes can also be deduced from the plots of the normalized film height as a function of flow rate, shown in Fig. 7. At low values, less than ≈ 1, of the parameters $\mathrm{Ha}\beta \sin\alpha$ and $\mathrm{Ha}\beta^2 \cos\alpha$, the β profile is indistinguishable from the nonmagnetic case. This is regime 1 flow, with only friction from the backing plate playing a role if β itself is $\ll 1$.

Deviation from OHD flow is seen when $\mathrm{Ha}\beta \sin\alpha > 1$, and full regime 2 is reached when $\mathrm{Ha}\beta \sin\alpha$ is both $\gtrsim 10$ and $\gtrsim \mathrm{Ha}\beta^2 \cos\alpha/2$. The value of 10 can be physically reasoned by setting the width of the Hartmann layer on the bottom wall to 1/10 the film height. In this case we have wide-channel, Hartmann flow due to the $\hat{y}$ component of the field, and we see a positive departure of the β profile from the nonmagnetic case. In this regime, assuming small β, we have

$$\beta = \frac{1 + [1 + 4Q(\mathrm{Ha}\sin\alpha)^3]^{1/2}}{2\mathrm{Ha}\sin\alpha} \approx (Q\mathrm{Ha}\sin\alpha)^{1/2} , \quad (45)$$

where the approximate relation is valid provided that $\mathrm{Ha}\sin\alpha \gg 1$.

The criterion for transition to regime 3 can also be determined by comparing the relative magnitudes of the two components of the magnetic forces $\mathrm{Ha}\beta \sin\alpha$ and $\mathrm{Ha}\beta^2 \cos\alpha$ used earlier. We see through this comparison that regime 3 is reached when $\mathrm{Ha}\beta^2 \cos\alpha$ is both $\gtrsim 100$ and $\gtrsim 2\ \mathrm{Ha}\beta \sin\alpha$ (the factor of 2 surfacing owing to the rectangular aspect ratio of the dimensionless solution space), the second inequality reducing to the conditions given in Eqs. (43) and (44). Regime 3 now is dominated in the core by the forces produced in response to the $\hat{z}$ component of the applied field. The value of the normalized film height can be approximately determined by the equation

$$\beta = Q\mathrm{Ha}\cos\alpha . \quad (46)$$

This relation describes linear β profiles that are nearly indistinguishable from the $\alpha = 0$ case, Eq. (42), for the small α values typical in a toroidal fusion reactor. Thus, for small angles, and this is seen in Fig. 7b, the value of β deviates from the $\alpha = 0$ case through regime 2 only, regimes 1 and 3 being very close to their $\alpha = 0$ counterpart. An analytic treatment of large Ha flows of this type is given in Roberts and Morley.[9] These asymptotic solutions are compared with and match well the preceding numerical results for open-channel flow, providing further confirmation of the numerical scheme.

IV.C. Electrically Conducting Walls

Once the conductivity of the walls is allowed to vary from zero, the flow can dramatically change from that of the purely insulated wall cases discussed earlier. In the programs FDFF and FDBV, the conductivity of the bottom and side walls can be varied separately, adding two more variable parameters, Φ_b and Φ_s.

$\alpha = 0$ Case

Beginning again with the field perfectly coplanar ($\alpha = 0$), we see for the low flow rates, and thus sufficiently small β, that little MHD interaction results. Typical velocity and field profiles are shown in Fig. 8, where Fig. 8a depicts the low interaction case.

As Q is increased and the film height rises, the currents circulating near the walls penetrate further into the center of the channel, and the MHD forces begin to affect the velocity profile. The velocity, like that seen in

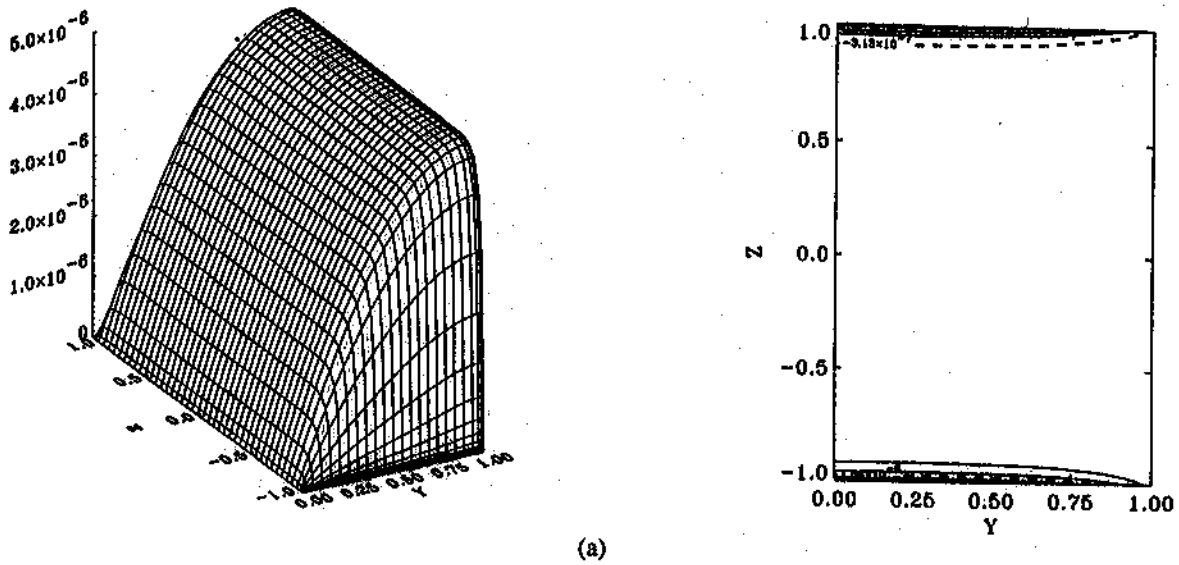

(a)

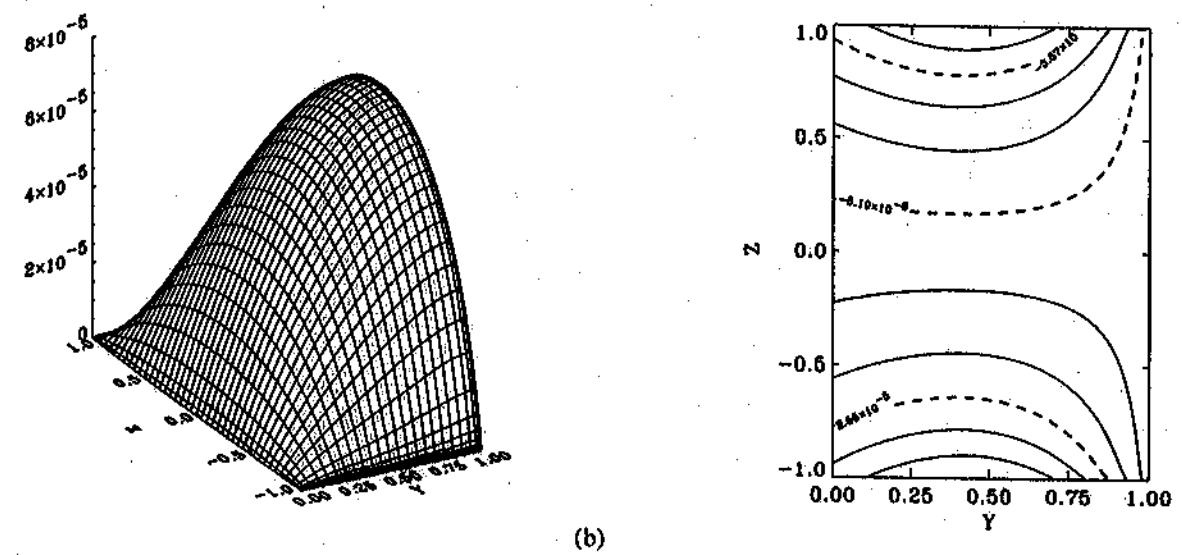

(b)

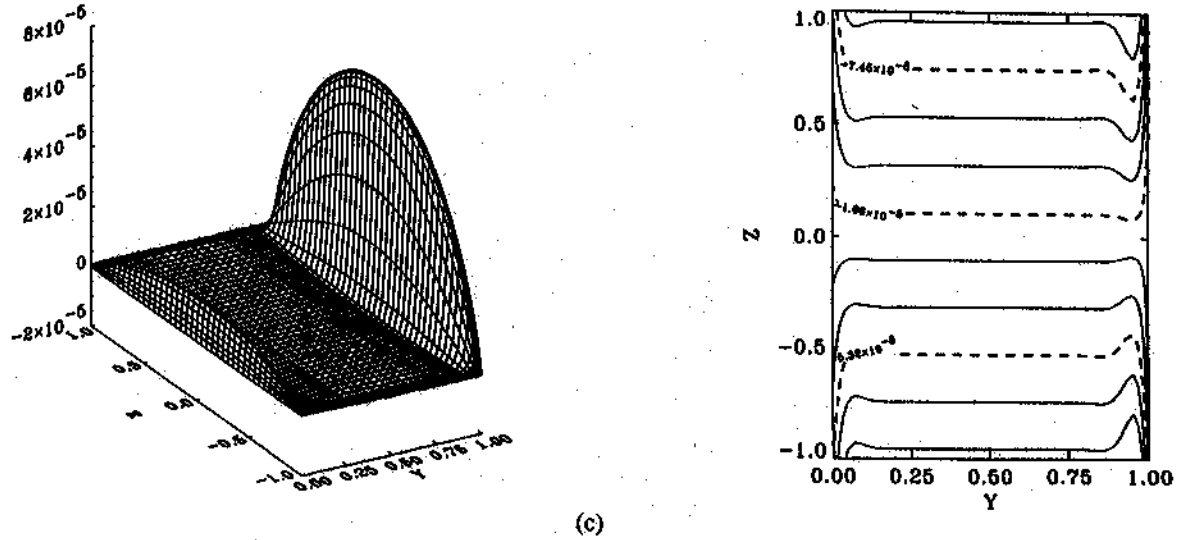

(c)

Fig. 8. Velocity and induced magnetic field profiles with Ha = 10^4, $\Phi_{s,b} = 0.01$, and Q = (a) 1×10^{-8}, (b) 5×10^{-7}, and (c) 1×10^{-6}.

Fig. 8b, gets more rounded in the affected area near the walls as MHD drag is larger where the majority of the current is circulating.

For values of $Ha\Phi_s > 10$, an interesting phenomenon is seen. As the flow rate is further increased from that of the case discussed earlier, the flow suddenly restructures into a flat core and boundary layer distribution, shown in Fig. 8c. This sudden restructuring is accompanied by an abrupt change in β. The grouping $Ha\Phi_s$ is approximately the ratio of the Hartmann current that returns through the channel side wall to that returning in the Hartmann layer. This rapid restructuring, then, is seen only for cases where $\gtrsim 90\%$ of the current returns in the side walls. For lesser ratios, the transition from one regime to the next is still a smooth one, although it changes very rapidly with Q.

The velocity pictured in Fig. 8c is typical of strong MHD interaction flows. The core velocity dips slightly before increasing into the large parallel layer velocity jets. Further increase in Q results in no change in the velocity profile aside from a thinning of the boundary layers and an increase in the relative magnitude of the velocity jets.

The induced field profile after reorganization becomes a linear function of z in the core region, indicating a constant core current in the $\hat{y}$ direction. As in the insulating wall case, again the current in the surface and bottom wall parallel layers first swerves toward the center of the channel before finally turning toward the walls. The presence of the free surface seems to exacerbate this effect.

All the cases pictured in Fig. 8 have $\Phi_s = \Phi_b$, but if the conductivity ratio of the bottom wall is allowed to differ from the side walls, the velocity and induced field profiles are affected. The velocity jet on the bottom wall is maximized when $\Phi_b = 0$ for a given Φ_s (see Fig. 9). The peak magnitudes of the velocity jets are approximately given by

$$v_{surf} = \frac{3}{4}\left(\frac{Ha\Phi_s}{1+\Phi_s}\right)\cdot v_{core} \tag{47}$$

and

$$v_{bot} = \frac{1}{4}\left(\frac{Ha\Phi_s}{1+\Phi_s}\right)\left(\frac{1}{1+\sqrt{Ha}\Phi_b}\right)\cdot v_{core} \tag{48}$$

at the surface and the bottom wall, respectively. As seen in Eq. (48), as Φ_b is increased from zero, the velocity jet in the parallel layer on the bottom surface drops in magnitude. As a larger portion of the current flows through the bottom wall, the velocity jet is effectively shorted out. The ratio of current in the bottom wall to current in parallel layer is given by $\sqrt{Ha}\Phi_b$, where at $\sqrt{Ha}\Phi_b = 1$ the current is evenly split between the two. At this value of Φ_b the boundary layer jet is reduced by half from its peak value at $\Phi_b = 0$. By $\sqrt{Ha}\Phi_b = 100$ the jet disappears entirely, as does the slight dip in the core velocity immediately adjacent to the jet and the bending of the core currents toward the center of the channel. The variation of Φ_b does not affect the magnitude of the surface jet, although it does cause a slight thinning of the surface jet thickness (see Fig. 9b). The value of Φ_b has no apparent effect on the Hartmann layers at all.

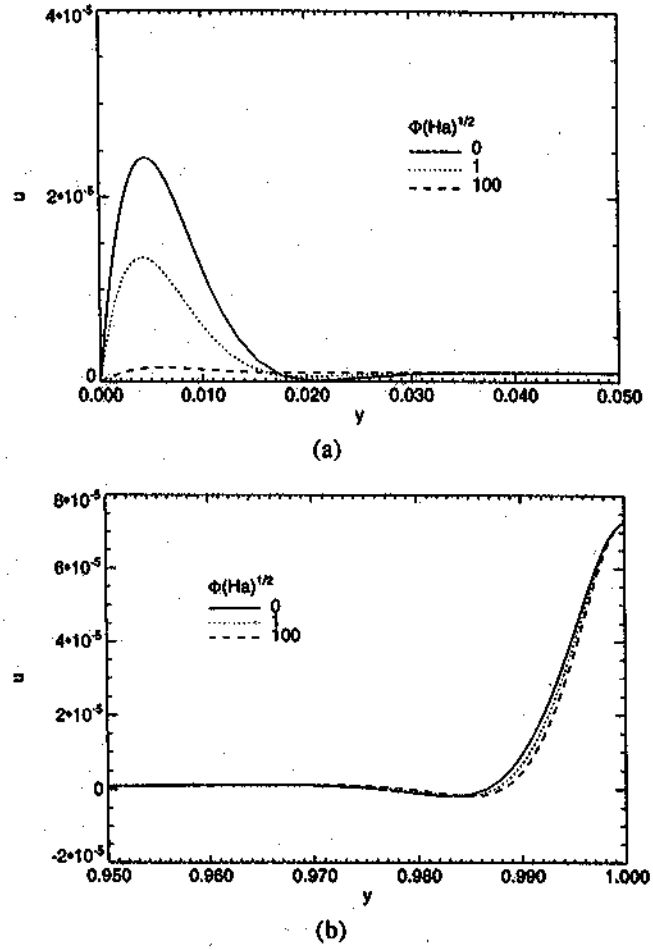

Fig. 9. Bottom wall and surface velocity parallel layers for different values of $\Phi_b Ha^{-1/2}$ at $Ha = 10^4$, $\Phi_s = 10^{-2}$, and $Q = 3 \times 10^{-6}$ ($\beta \sim 1.9$).

The magnitude of the velocity jets, along with the parallel layer thickness, can be used to estimate the percent of flow in the core and in the side layers. We define the following approximate flow quantities:

$$q_{surf} = 2k_s \frac{3}{4}\left(\frac{Ha\Phi_s}{1+\Phi_s}\right)\frac{k_t}{(Ha\beta^2)^{1/2}}\cdot v_{core}\ , \tag{49}$$

$$q_{bot} = 2k_s \frac{1}{4}\left(\frac{Ha\Phi_s}{1+\Phi_s}\right)\frac{k_t}{(Ha\beta^2)^{1/2}} \times \left(\frac{1}{1+\sqrt{Ha}\Phi_b}\right)\cdot v_{core}\ , \tag{50}$$

and

$$q_{core} = 2 \cdot v_{core} , \tag{51}$$

where the constants k_s and k_t are geometric factors that account for the average shape and thickness of the jets, respectively. These flow rates can be used to determine the approximate ratio of flow in each of the areas to the total flow. The percent in the core is given by

$$\%\ \text{flow in core} = \frac{\beta}{k_s k_t \dfrac{\Phi_s \sqrt{\text{Ha}}}{1 + \Phi_s}\left[1 - \dfrac{\Phi_b \sqrt{\text{Ha}}}{4(1 + \Phi_b \sqrt{\text{Ha}})}\right] + \beta} . \tag{52}$$

The product $k_s k_t$ is empirically determined to be $\sim\frac{8}{9}$. This numerical result is consistent with a thickness factor of ~2 (which itself is consistent with the parallel layer jet thicknesses seen in Fig. 9) and a shape factor of $\frac{2}{3} \cdot \frac{2}{3}$, resulting from a two-dimensional parabolic average.

The value of β for cases of relatively strong MHD interaction can be determined by solving the Hartmann problem for the case of side walls of infinite extent and including the flow quantity expected in the parallel layer jets:

$$\beta = Q\text{Ha}\left(\frac{1 + \text{Ha}\Phi_s}{1 + \Phi_s}\right) - \frac{8}{9}\frac{\Phi_s \sqrt{\text{Ha}}}{1 + \Phi_s}\left[1 - \frac{\Phi_b \sqrt{\text{Ha}}}{4(1 + \Phi_b \sqrt{\text{Ha}})}\right] . \tag{53}$$

[This equation is easily substituted into Eq. (52) to determine the flow percentage in the core as function of Ha, Q, and Φ.] Figure 10a shows β profiles in a channel with conducting side walls for different values of Ha, from which we can see that in the region of strong interaction the β profile is a linear function of Q, which is well predicted by Eq. (53). The recent treatment of this problem by Shishko[7] gives the following relation:

$$\beta = Q\text{Ha}\left(\frac{1 + \text{Ha}\Phi_s}{1 + \Phi_s}\right) - \frac{1}{9}\left(\frac{1}{\sqrt{\text{Ha}}} + \frac{\Phi_b}{1 + \Phi_b \sqrt{\text{Ha}}}\right) - \frac{8}{9}\frac{\Phi_s \sqrt{\text{Ha}}}{1 + \Phi_s}\left[1 - \frac{\Phi_b \sqrt{\text{Ha}}}{3(1 + \Phi_b \sqrt{\text{Ha}})}\right] , \tag{54}$$

which appears to be in slightly better agreement with the numerical results near the jump region. Both reduce to the insulated wall case, Eq. (42), when $\Phi_s, \Phi_b \to 0$ and $\text{Ha} \to \infty$.

Also in Fig. 10, we see that β begins to deviate from the OHD prediction again at $\text{Ha}\beta_{ohd}^2 \approx 1$, with the jump in β occurring at slightly higher values. Upon closer examination of the behavior of β close to Q_{jump}, we can see that a region with multiple values of β exists (see Fig. 11). If small steps in Q are taken with the FDBV

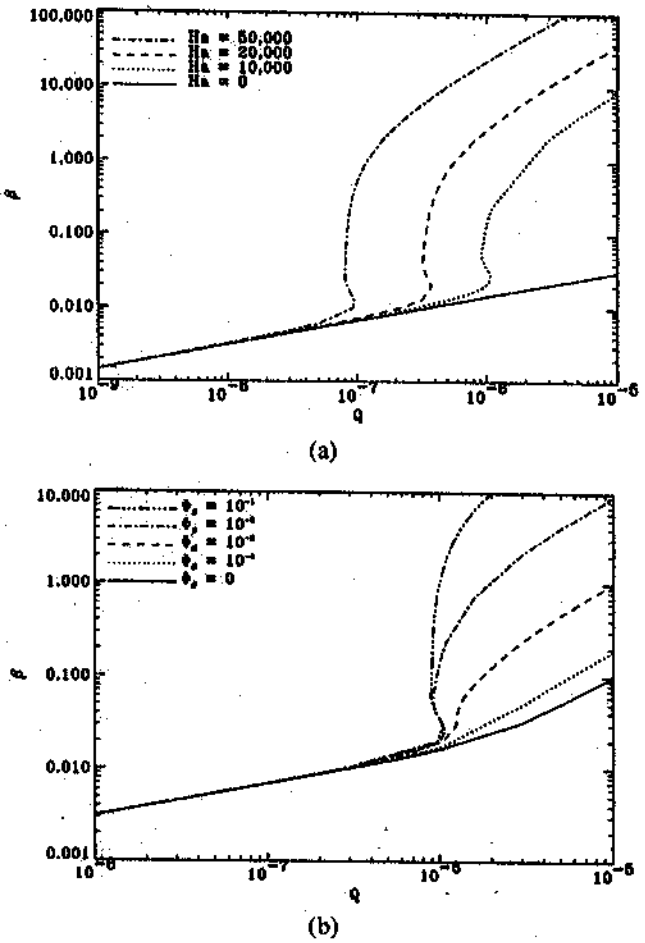

Fig. 10. Normalized film height as a function of flow rate for (a) various Ha at $\Phi_s = 0.01$, and (b) various Φ_s at $\text{Ha} = 10^4$ with $\alpha = \Phi_b = 0$.

code and if the previous step's data are used as an initial guess, different values of β are predicted depending on whether Q_{jump} is approached from above or below. This region of multiple values is a result of the nonlinear nature of β in the coupled, governing equations. This phenomenon was first predicted by Shishko[7] in his approximate treatment. Although not mentioned by Walker, his exact solution for cases with perfectly conducting side walls and an insulated bottom wall[3] predicts this behavior as well.

The intermediate values of β, seen in Fig. 11 between the upper and lower values in the multivalued region, are, in principle, impossible to reach. Thus, a range of unattainable uniform film heights is created since a flow increasing in Q would suddenly jump to the upper β at Q_{jump} and likewise would jump from the upper to the lower β as Q was decreased. This hysteresis around the Q_{jump} region also is a maximum when $\Phi_b = 0$ and gets gradually smaller, disappearing along with the bottom wall velocity jet at $\Phi_b \sqrt{\text{Ha}} \approx 100$. In other words,

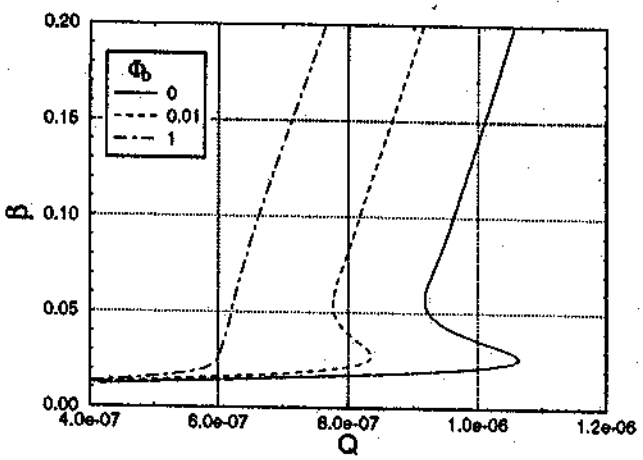

Fig. 11. Normalized film height as a function of flow rate near Q_{jump} in a conducting channel ($\Phi_s = 10^{-2}$) for various Φ_b and Ha = 10^4.

the hysteresis disappears when the bottom wall carries nearly all the parallel current and the bottom jet is completely suppressed.

The width of the hysteresis region appears to vary with Φ_b as $(1 + \Phi_b\sqrt{\text{Ha}})^{-1}$ times the width at $\Phi_b = 0$. Thus, the range of multiple β gets smaller with increasing $\Phi_b\sqrt{\text{Ha}}$. A general tendency seems to be that the unattainable region is approximately centered around the point when $\text{Ha}\beta^2 = 10$. Thus, typically β's in the region around

$$\beta = \left(\frac{10}{\text{Ha}}\right)^{1/2} \tag{55}$$

cannot be realized. It is approximately at this β that the upper and lower branches of β join as $\Phi_b\sqrt{\text{Ha}}$ is increased to the point where hysteresis disappears.

$\alpha \neq 0$ Case

At this point in the discussion all the variable parameters are included, and the practicality of scanning the entire parameter space is somewhat limited. Two cases with $\alpha = 5$ deg, shown in Figs. 12 and 13, are given as typical.

1. 1case A:
   a. moderately conducting side walls ($\Phi_s = 10^{-2}$)
   b. insulated bottom wall
2. 2case B:
   a. moderately conducting bottom wall ($\Phi_b = 10^{-2}$)
   b. insulated side walls.

The cases are shown in the figures for several different values of β instead of Q since the two cases respond much differently as functions of Q. As in the previous $\alpha \neq 0$ case discussed in Sec. IV.B, we again find it convenient to demarcate the channel into three regions: I, II, and III, shown in Fig. 2. Also, the concept of flow regimes 1, 2, and 3 is again used to describe OHD, $\hat{y}$ field dominated, and $\hat{z}$ field dominated regimes, respectively.

At low flow rates (low β) the flow is in regime 1 and so is largely unaffected by the field. As the flow rate increases, and β with it, regime 2 is entered. As in the equivalent insulated wall, $\alpha \neq 0$ case (see Sec. IV.B), deviation from regime 1 begins at about $\text{Ha}\beta \sin\alpha \approx 1$, and the flow is fully in regime 2 at $\text{Ha}\beta \sin\alpha \approx 10$. This regime is seen in Figs. 12a and 13a for the different wall conductance cases defined earlier. Notice that region I looks like flat, Hartmann flow resulting from the $\hat{y}$ field component but that the parallel layers separating the regions can contain large velocity jets, especially when the bottom wall is conducting. The presence of artificial diffusion is seen in these jets since the field is oblique to the numerical grid. The dip in the interior region of the large jet of Fig. 13a is due in part to the smearing out of the jet in the interior region, a consequence of the wider grid spacing there as compared with the near-wall regions. The velocity jets are at maximum magnitude when $\Phi_s = 0$ and tend to be shorted out as Φ_s increases.

The isolines of induced field for regime 2, also pictured in Figs. 12a and 13a, give the paths of electric current circulation. In region I the current is oriented perpendicular to the $\hat{y}$ field, not to the total field. In Fig. 12a the Hartmann layer return current path is clearly seen on the bottom wall. This layer is not as easily seen in Fig. 13a since most of the current returns through the conducting bottom wall. We see for case B, though, a local cell of recirculation in the lower left corner of the channel. The currents leaving region III and entering region I bend around this cell, resulting in a current component in the $+\hat{y}$ direction, which accelerates the film and causes the velocity jets to form. As the current leaves region I and enters region II, the currents begin to turn toward the bottom wall. This is especially apparent in case B (Fig. 13a), where the bottom wall carries the majority of the current back to the $z = -1$ side wall. This current in the $-\hat{y}$ direction suppresses the velocity in region II, making it small here compared with the region I velocity. Some current closes through the near side wall too, especially in Fig. 13a, so that region II has two oppositely circulating current cells.

As β increases further, we approach the point where $\beta = 2\tan\alpha$, and the flow is in transition from regime 2 to 3. Near-transition flows are shown in Figs. 12b and 13b. For case B, the flow is mostly in the parallel layers, while case A results in a large flow quantity still in the thin region I. The currents in region I still try to remain perpendicular to the $\hat{y}$ field but are more bent, especially in case A.

Further β increase moves us firmly in regime 3, pictured in Figs. 12c and 13c for our two test cases. For case A, the flow looks like the peaked velocity jets

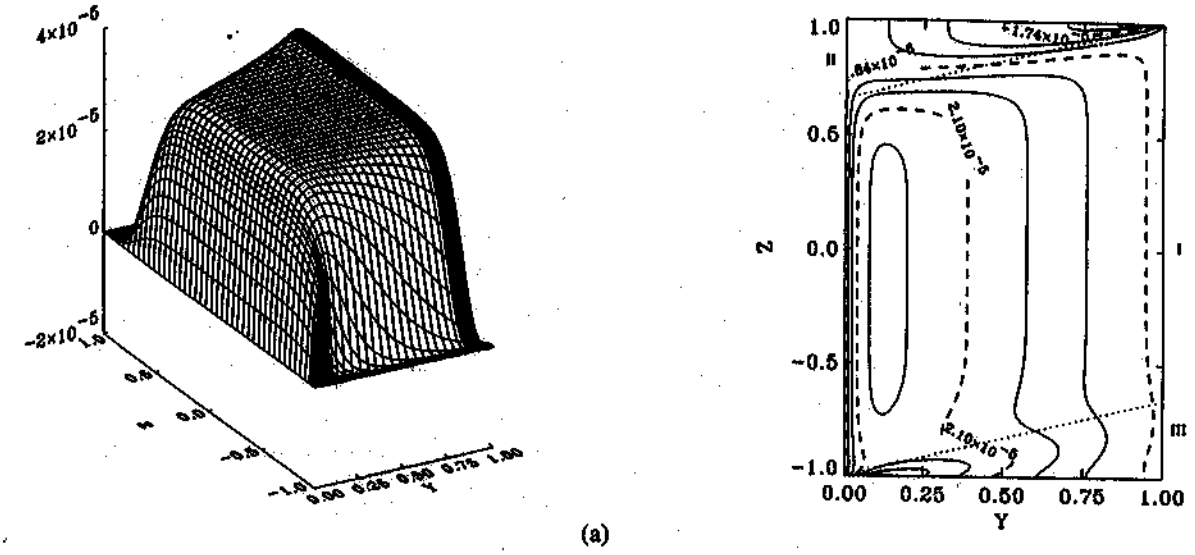

(a)

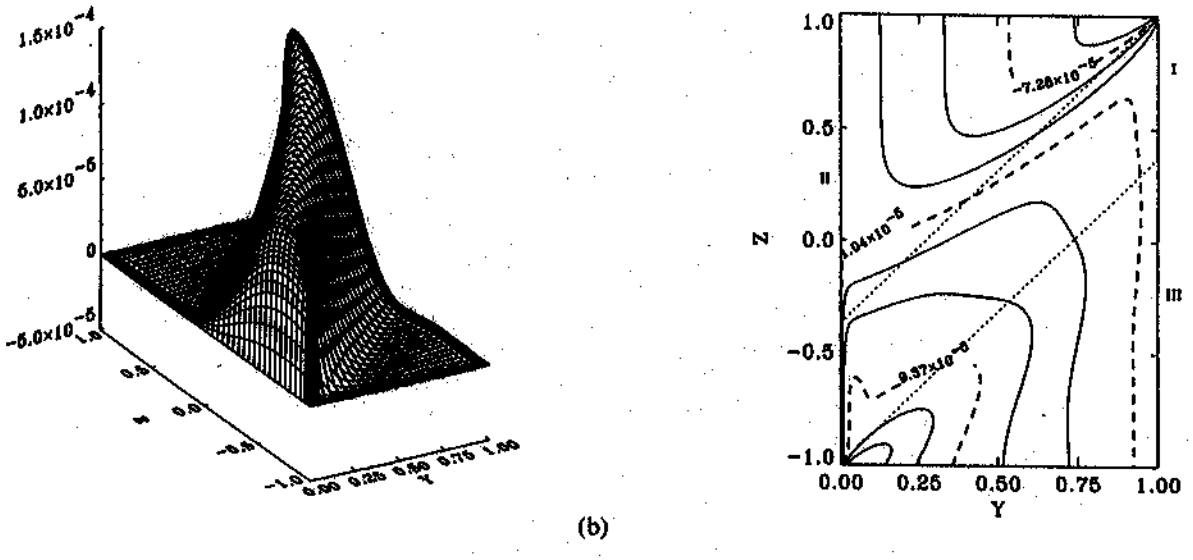

(b)

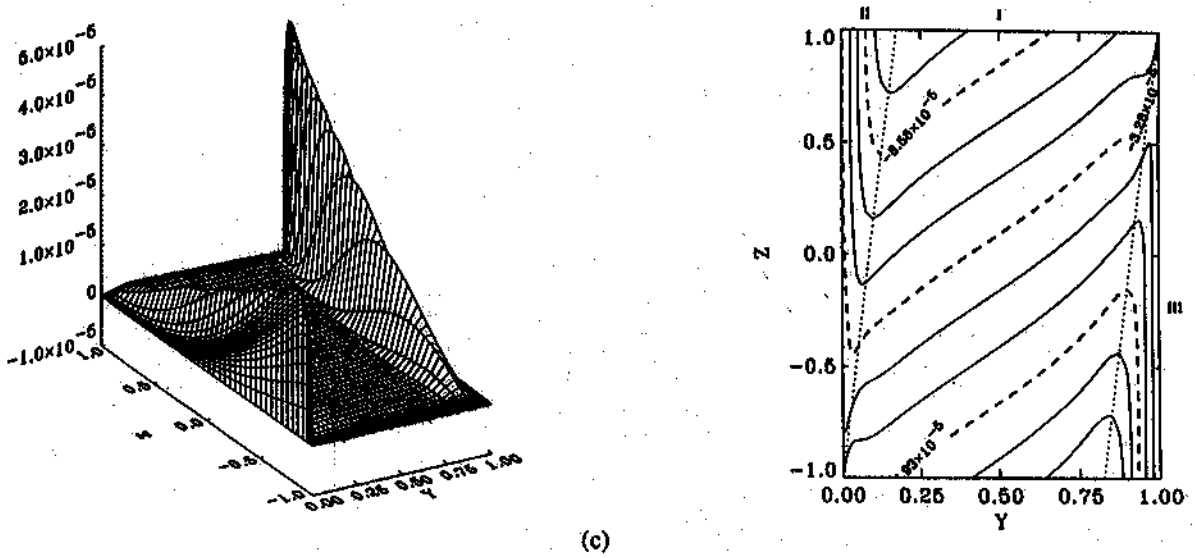

(c)

Fig. 12. Velocity and induced magnetic field profiles with Ha = 10^4, $\Phi_s = 0.01$, $\Phi_b = 0$, and $\alpha = 5$ deg at (a) $\beta = 0.03$, (b) $\beta = 0.12$, and (c) $\beta = 1$.

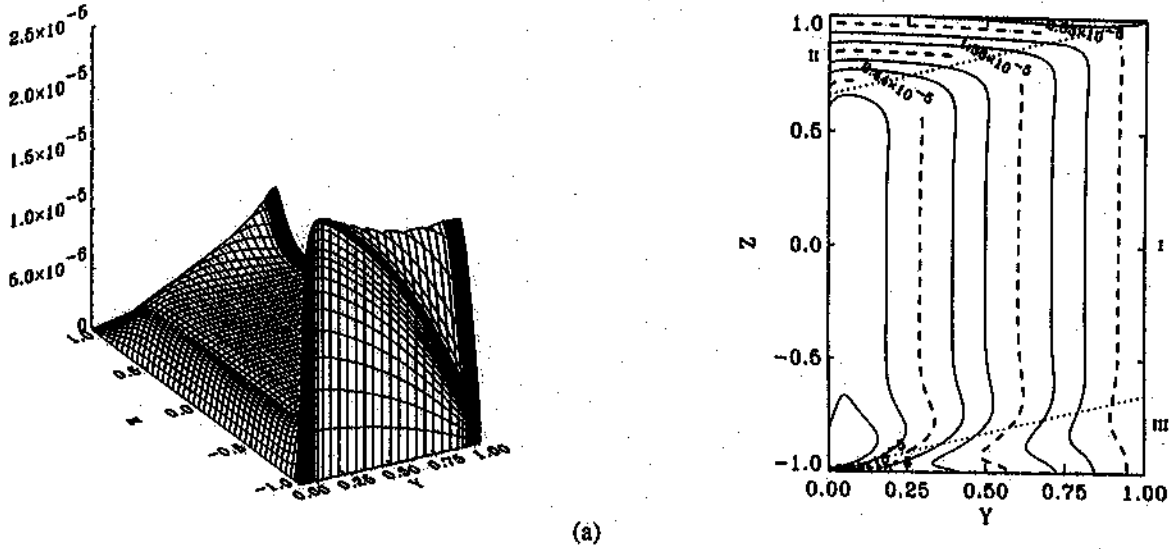

(a)

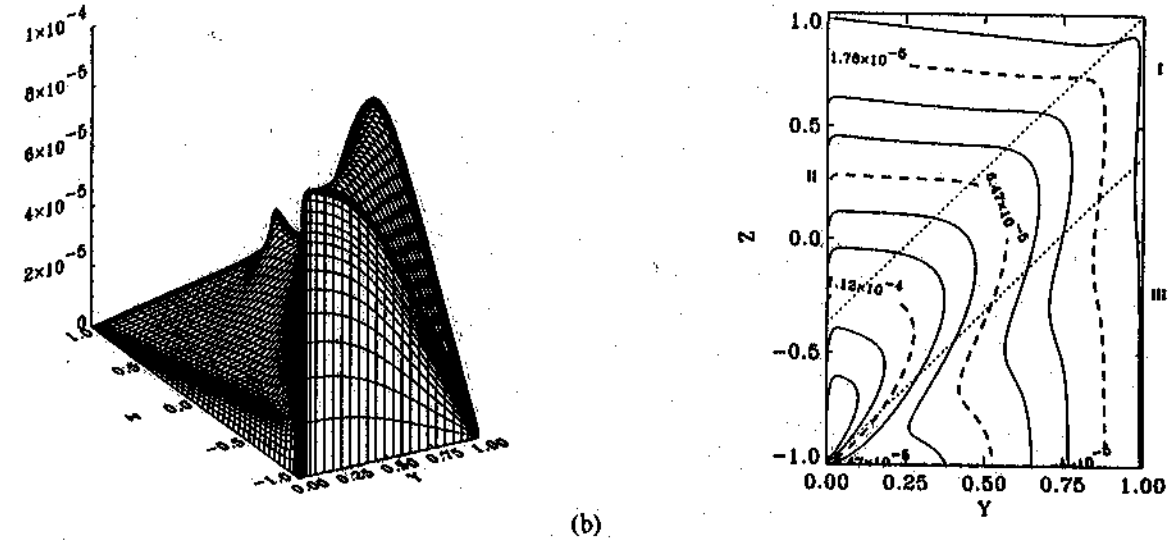

(b)

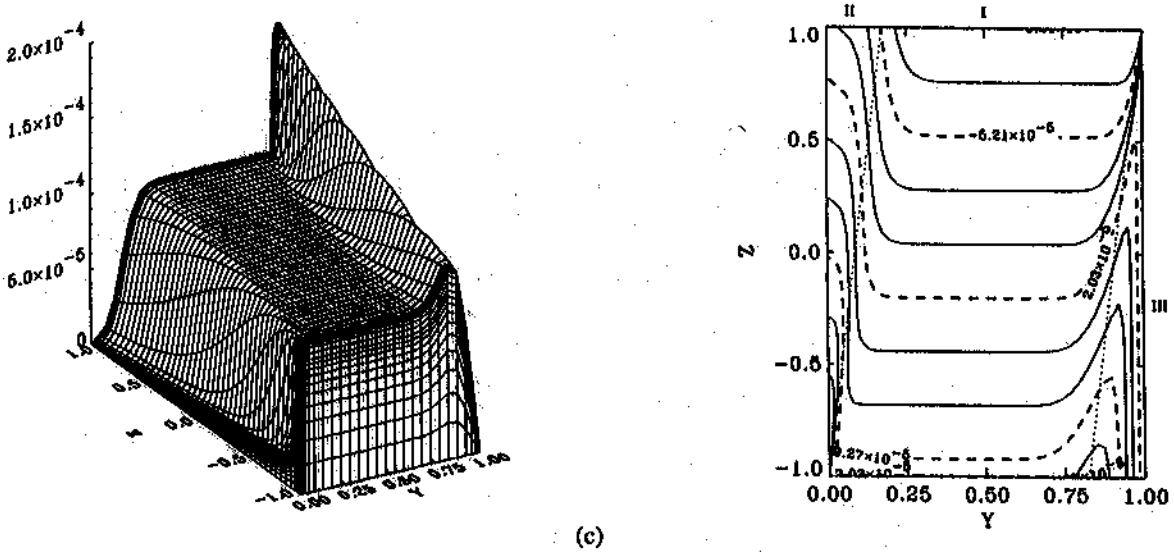

(c)

Fig. 13. Velocity and induced magnetic field profiles with Ha = 10^4, $\Phi_b = 0.01$, $\Phi_s = 0$, and $\alpha = 5$ deg at (a) $\beta = 0.03$, (b) $\beta = 0.12$, and (c) $\beta = 1$.

indicative of the $\alpha = 0$, conducting walls cases (discussed earlier in this section), except the shape of the jets is more triangular than parabolic. The jet on the bottom wall can be shorted out if Φ_b is increased and Φ_s is held constant. In case B, the flow looks more like the nonconducting wall cases since the bottom wall conductivity alone has little effect on $\alpha = 0$ flow with insulated side walls.

The currents in regime 3 behave a little oddly for case A. They traverse region I at an acute angle to the dominant $\hat{z}$ field instead of perpendicular to it. This means that there is less $j \times B$ drag than in the purely $\alpha = 0$ case. As β continues to increase, the current lines become more perpendicular to $\hat{z}$ but near the free surface still bend toward the field. This trend is not seen in the Fig. 13c current profile. Less MHD drag results in a smaller β for a given Q in region 3 than would be predicted by substituting $\mathrm{Ha}\cos\alpha$ for Ha into the formulas for β given for the $\alpha = 0$, conducting wall cases [see Eq. (53)]. Only at very large β will this substitution give a good estimate.

Looking at Fig. 14, plots of the β and Q profiles for the same two test cases, we see that the profiles can behave very differently, depending on the wall conductance arrangement. In regime 2 (defined previously as $\mathrm{Ha}\beta\sin\alpha > 10$ and $> \mathrm{Ha}\beta^2\cos\alpha/2$), β is given by the relation (for small β)

$$\beta = \big(1 - \mathrm{Ha}\Phi_b\sin\alpha + \{(1 + \Phi_b\mathrm{Ha}\sin\alpha)[1 + \Phi_b\mathrm{Ha}\sin\alpha + 4Q(\mathrm{Ha}\sin\alpha)^3]\}^{1/2}\big)/(2\mathrm{Ha}\sin\alpha)\ , \quad (56)$$

which reduces to Eq. (45) as $\Phi_b \to 0$. Since the friction with the bottom wall is included in its derivation, Eq. (56) is accurate provided only that $\tanh[\mathrm{Ha}\beta\sin\alpha] \approx 1$.

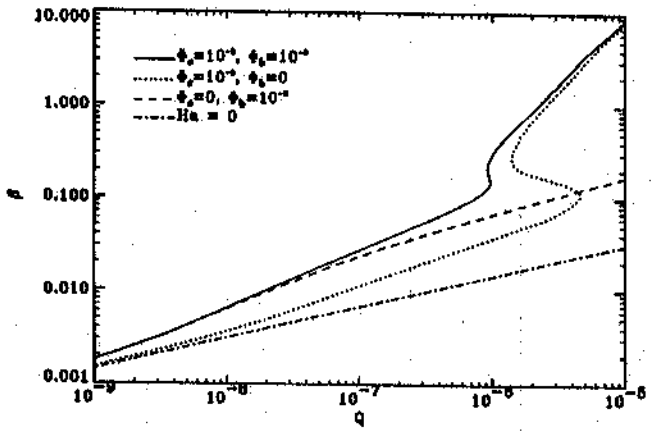

Fig. 14. Normalized film height as a function of flow rate for $\mathrm{Ha} = 10^4$, $\alpha = 5$ deg, and various wall conductances.

The conductivity of the side walls affects regime 2 flow by suppressing the velocity jets, causing a thickening of the film as compared with completely insulated side walls with a conducting backplate. In the range of flow rates pictured (Fig. 14), regime 3 flow is not even reached in case B, even though $\mathrm{Ha}\beta^2\cos\alpha \approx 100$. This is because the $\beta = 2\tan\alpha$ point is not reached and the $\hat{y}$ field still dominates.

Multivalued regions of β, clearly seen in Fig. 14, still occur for cases where the side walls carry a large portion of the current. The jump now occurs between regimes 2 and 3, not between OHD and MHD regimes discussed in the $\alpha = 0$ flow. For case A, the multivalued region is drawn out significantly (26 times) from the $\alpha = 0$ case with the same parameters. The case B transition from regime 2 to 3 flow (not pictured) has no multivalued region. This is to be expected since, as mentioned previously, it behaves like an insulated channel in regime 3, with the conductivity of the bottom wall having little effect on the core flow.

V. CONCLUSIONS

The examination of fully developed, open-channel flow in a magnetic field has revealed several interesting phenomena. The factor $\mathrm{Ha}\beta^2$, owing to the different length scales in a wide thin film, is the parameter that indicates the ratio of magnetic to viscous forces for flows where the magnetic field is exactly coplanar. The first effects of the magnetic forces are observed at values of this parameter near one, while inviscid MHD core flow has developed by $\mathrm{Ha}\beta^2 \approx 100$.

In completely insulated channels, there is a parabolic velocity jet at the free surface, which is essentially a parallel layer restrained only by friction at the side walls. The peak magnitude of this jet is equal to the constant core velocity multiplied by $\sqrt{3}$.

In channels with nonzero electrical conductivity, the inviscid core flow is accompanied by boundary-layer velocity jets that can carry an appreciable portion of the flow. The peak magnitude of these jets is not a constant multiple of the core velocity but a function of Ha and the wall conductance. Modification of the basic Hartmann core flow approximation to include these jets is necessary to accurately predict the value of the uniform film height as a function of the flow parameters. The channel conductivity also causes the formation of a region of multiple values of β for the same flow rate, with the behavior of the film differing, depending on whether the Q_{jump} region is approached from greater or lesser values of Q.

When the channel is at an oblique angle α to the magnetic field, the inviscid core flow can behave in two different fashions. The reduction of α to below arctan $\beta/2$ results in flow that behaves predominately as the purely coplanar case with a Hartmann number based on the $\hat{z}$ component of the field, $\mathrm{Ha}\cos\alpha$. Above this limit in α,

TABLE I

Summary of Flow Regime Behavior

	Regime 1	Regime 2	Regime 3
Definition	$1 > \mathrm{Ha}\beta^2\cos\alpha$, $\mathrm{Ha}\beta\sin\alpha$	$\mathrm{Ha}\beta\sin\alpha > 10$, $\frac{1}{2}\mathrm{Ha}\beta^2\cos\alpha$	$\frac{1}{2}\mathrm{Ha}\beta^2\cos\alpha > 50$, $\mathrm{Ha}\beta\sin\alpha$
Description	Region I dominated by viscous forces	Region I dominated by B_y	Region I dominated by B_z
β relationship	Eq. (41) when $\beta \ll 1$	Eq. (45) or (56), depending on α and Φ	Eq. (46) or (54), depending on α and Φ

the flow is dominated by the $\hat{y}$ component of the field, even if it is considerably lesser in magnitude than the $\hat{z}$ component. The parameter governing the ratio of magnetic to viscous forces in this case is $\mathrm{Ha}\beta\sin\alpha$. This fact has serious implications for the modeling of fusion relevant flows,[8] especially those that rely on the assumption of a Hartmann distribution of velocity and/or electric current across the coplanar direction.

The behavior of the different flow regimes is summarized in Table I. The approximate relations for β noted in the table are quite accurate for insulated channel walls due to small amount of flow in parallel layer velocity jets. When walls are conducting, the relations for regime 3 are more accurate for the $\alpha = 0$ cases since the jet magnitude has been determined and is included in the derivation. Cases when $\alpha, \Phi \neq 0$ are the least accurate of these approximate formulas.

NOMENCLATURE

a = channel width with side walls at $\pm a/2$ (m)

$B^{i,a}$ = induced or applied magnetic induction (T)

b_* = characteristic induced magnetic field, $u_*\mu(\sigma\rho\nu)^{1/2}$ (T)

g = acceleration of gravity vector (m/s^2)

Ha = Hartmann number, $B(a/2)(\sigma/\rho\nu)^{1/2}$

h = uniform film height (m)

i,j = numerical grid indices in y and z

Pe = cell Peclet number, $u\delta/\alpha_d$

Q_* = characteristic flow rate, $2(a/2)^2u_*$ (m^3/s)

u_* = characteristic velocity, $(a/2)^2 g\sin\theta/\nu$ (m/s)

y_*, z_* = characteristic lengths, h and $a/2$

Greek

α = angle of applied field to $\hat{z}$

β = normalized film height, $h/(a/2)$

$\delta_{y,z}$ = computational grid spacing

$\Phi_{s,b}$ = wall conductance ratio, $(\sigma_{s,b}\, a_{s,b})/[\sigma_f(a/2)]$

θ = angle of channel slope to horizon

$\omega_\pm$ = fully developed flow functions, $\tilde{u} \pm \tilde{b}_x$

ACKNOWLEDGMENTS

The authors wish to thank Mark S. Tillack and Rachel S. Bennahum for many helpful discussions and editorial suggestions. This work was partially supported by a Magnetic Fusion Energy Technology Fellowship administered for the U.S. Department of Energy by the Oak Ridge Institute for Science and Education.

REFERENCES

1. B. BADGER et al., "Wisconsin Torodial Fusion Reactor Design Study," Technical Report UWFDM-68, Vol. 2, p. III-D-1, University of Wisconsin, Madison (1974).

2. R. A. ALPHER, H. HURWITZ, Jr., R. H. JOHNSON, and D. R. WHITE, "Some Studies of Free Surface Mercury Magnetohydrodynamics," *Rev. Mod. Phys.*, **32**, *4*, 758 (1960).

3. J. S. WALKER, "Uniform Open Channel Liquid Metal Flows with Transverse Magnetic Fields," *Proc. 14th Midwestern Mechanics Conf., Developments in Mechanics*, Vol. 8, p. 421 (1975).

4. P. R. HAYS and J. S. WALKER, "Liquid-Metal MHD Open-Channel Flows," *J. Appl. Mechan.*, **51**, 13 (1984).

5. T. N. AITOV, A. B. IVANOV, and A. V. TANANAEV, "Flow of Liquid Metal in a Chute in a Coplanar Magnetic Field," *Magnetohydrodynamics*, **23**, *1*, 91 (1987).

6. I. A. EVTUSHENKO, S. Y. SMOLENTSEV, and A. V. TANANAEV, "Hydrodynamics and Exchange of Heat in Thin Liquid-Metal Layers Within a Magnetic Field," *Magnetohydrodynamics*, **27**, *3*, 287 (1991).

7. A. SHISHKO, "A Theoretical Investigation of Steady-State Film Flows in a Coplanar Magnetic Field," *Magnetohydrodynamics*, **28**, *2*, 170 (1992).

8. N. B. MORLEY and M. A. ABDOU, "Modeling of Fully-Developed, Liquid Metal, Thin Film Flows for Fusion Divertor Applications," *Fusion Eng. Des.*, **30**, 339 (1996).

9. P. ROBERTS and N. B. MORLEY, "Solutions of Uniform, Open-Channel, LM-MHD Flow in a Strong, Oblique Magnetic Field," *Phys. Fluids*, **8**, *4* (1996).

10. N. B. MORLEY, "Numerical and Experimental Modeling of Liquid Metal, Thin Film Flow in a Quasi-Coplanar Magnetic Field," PhD Thesis, University of California, Los Angeles (Dec. 1994).

11. V. M. KUDRIN, S. Y. SMOLENTSEV, and A. V. TANANAEV, "Developed Flow of a Thin Liquid Metal Layer in an Inclined Magnetic Field," *Magnetohydrodynamics*, **29**, *1*, 66 (1993).

12. J. A. SHERCLIFF, *A Textbook of Magnetohydrodynamics*, Pergamon Press Ltd., London (1965).

13. S. PATANKAR, *Numerical Heat Transfer and Fluid Flow*, McGraw-Hill Book Company, New York (1981).

Neil B. Morley [BS, electrical engineering, University of New Mexico, 1988; MS, 1990, and PhD, 1994, nuclear engineering, University of California, Los Angeles (UCLA)] is currently a U.S. Department of Energy fusion technology postdoctoral fellow at UCLA. He works on a variety of fusion energy technology problems for both magnetic and inertial confinement fusion, including duct and thin-film flow MHD, open flows for inertial fusion cavity protection, and International Thermonuclear Experimental Reactor test blanket design and analysis (in conjunction with the French Commissariat à l'Energie Atomique, Saclay).

Mohamed A. Abdou is a professor in the Department of Mechanical, Aerospace, and Nuclear Engineering at UCLA and also is the director of fusion technology at UCLA. His research interests include neutronics, thermomechanics, fusion technology, and reactor design and analysis.